Check for updates

Influence of aluminum zoning toward external surfaces in MFI zeolites on propene oligomerization catalysis†

Ricem Diaz Arroyo, Young Gul Hur and Rajamani Gounder ⬡ *

Brønsted acid zeolites catalyze alkene oligomerization reactions, an important route to produce fuels and chemicals from light hydrocarbon feedstocks. Propene dimerization rates (per H⁺, 503 K) decrease monotonically with increasing crystallite size in MFI zeolites because heavy oligomer products remain occluded within microporous voids and restrict intrazeolite diffusion of reactants and products. Here, we show that the preferential zoning of framework Al centers and their associated H⁺ sites toward exterior surfaces of MFI crystallites in an "egg-shell" architecture minimizes the extent of diffusion-enhanced secondary reactions within a given crystallite, which increases both propene dimerization rates (per H⁺) and selectivity to true oligomer products. These results show that tailoring Al distributions to be spatially zoned toward external surfaces of medium-pore zeolite crystallites is efficacious at minimizing diffusion path lengths to increase alkene oligomerization rates and selectivity to true oligomer products.

Zeolites are inorganic crystalline frameworks that confine acid sites (H⁺) within microporous voids. Brønsted acidic zeolites are used to convert carbon-based feedstocks to fuels and chemicals *via* routes such as methanol to hydrocarbons (MTH),[1] alkene (C_{6+}) cracking to smaller hydrocarbons,[2] and alkene (C_2–C_5) oligomerization to larger fuel-range molecules.[3–6] These routes involve complex reaction networks wherein measured reaction and deactivation rates and product selectivity are influenced by coupled reaction–diffusion phenomena at the zeolite crystallite scale, described by the Thiele modulus (Φ):[7,8]

$$\Phi^2 \propto \frac{k}{D_e} \Psi \qquad (1)$$

Charles D. Davidson School of Chemical Engineering, Purdue University, 480 Stadium Mall Drive, West Lafayette, IN 47907, USA. E-mail: rgounder@purdue.edu
†Electronic supplementary information (ESI) available. See DOI: https://doi.org/10.1039/d4dt01530d

where k is the effective kinetic rate constant, D_e is the effective diffusivity, and Ψ is a lumped diffusion parameter defined as:

$$\Psi = [H^+]L^2. \qquad (2)$$

The diffusion parameter (Ψ) combines two material structural properties of the inorganic zeolite framework that influence coupled reaction–diffusion within a single crystallite, the volumetric proton density ($[H^+]$) and the characteristic diffusion path length (L).[8–10] If the H⁺-site density is assumed to be homogeneously distributed throughout the zeolite crystallite volume, L is typically taken as half the crystallite size (*e.g.*, radius for a spherical particle) along the direction imposing the weakest resistance to intracrystalline diffusion. Increasing values of Ψ lead to decreasing reaction rates in coupled reaction–diffusion systems, as shown by Bickel *et al.* for propene oligomerization rates (per H⁺, 503 K, 315 kPa C_3H_6) that decreased systematically with increasing crystallite size (0.13–2.65 μm) on MFI zeolites of fixed H⁺-site density (Si/Al = 250).[8]

Increasing values of Ψ also strongly influence measured product selectivities, as shown by Sarazen *et al.* who studied the influence of intracrystalline diffusional constraints imposed by the inorganic zeolite framework (*e.g.*, undulation factor, pore dimensionality, crystallite size) on propene oligomerization catalysis (75 kPa C_3H_6, 503 K).[7] The true oligomer selectivity (χ, eqn (3)) describes the fraction of all carbon atoms in converted propene reactants that are retained in true oligomer products that egress from the catalyst bed before undergoing β-scission:

$$\chi = 1 - \frac{r_\beta}{r_{oligo}} \qquad (3)$$

where r_β is the total rate of formation of all species with carbon atoms that are non-integer multiples of the reactant (3 carbon atoms in propene) and r_{oligo} is the total rate of formation of true oligomers (*e.g.*, C_6, C_9, C_{12}). The MFI topology has three-dimensional pore connectivity containing large

channel intersections (~0.70 nm diameter) that allow the formation of large oligomers whose diffusion is restricted by smaller channels (~0.55 nm diameter), thus favoring β-scission events to form smaller oligomers that more readily diffuse through smaller apertures in the microporous network.[7] Among commercial MFI samples (Si/Al = 14–140), the true oligomer selectivity decreases systematically as Ψ increases because of increased extents of diffusion-enhanced secondary reactions (e.g., β-scission).[7] In contrast, zeolites with one-dimensional pore topologies without undulation (e.g., TON) prevent the formation of oligomers that would be too large to diffuse out of the microporous network and thus lead to true oligomer selectivity close to unity (~0.8–1).[7] In addition, Noh et al. observed significant differences in product selectivity during isomerization and β-scission reactions of 2,4-dimethylpentane and n-heptane (H_2/alkane = 2.5–300, 548 K, <10% alkene conversion) among mesoporous materials (MCM-41), large-pore (12-MR: MCM, FAU, BEA) and medium-pore (10-MR: SVR, MFI, MEL) zeolites.[11] The selectivity to isomerization and β-scission was independent of zeolite topology in mesoporous materials and large-pore zeolites, while medium-pore zeolites with undulations are influenced by secondary reactions that favor β-scission products, which increases the selectivity to β-scission of primary isomers on their way out of crystallites.[11]

Synthetic methods to alleviate diffusional constraints typically rely on decreasing L by decreasing the crystallite size, introducing mesoporous voids within microporous crystallites to create hierarchical pore networks, and preparing two-dimensional sheet-like materials and other related architectures.[12–17] Zeolites, however, often contain Al distributions that are spatially heterogeneous throughout the crystallite volume and at external crystallite surfaces, and such heterogeneities have been reported to influence reaction and deactivation rates and product selectivity for various Brønsted acid-catalyzed reactions.[16,18–22] Le et al. crystallized a suite of MFI samples with varied spatial distributions of Al, both enriched and depleted at external surfaces, and crystallite sizes (1.1–12.0 μm) using a mixture of tetrapropylammonium (TPA^+), Na^+ and K^+ structure-directing agents (SDAs) at various crystallization temperatures (373–463 K).[22] Longer catalyst lifetimes and higher product selectivity to ethene (relative to the sum of 2-methylbutane and 2-methyl-2-butene) during MTH reactions (11.5 kPa CH_3OH, 673 K) were measured for MFI samples with Al enriched toward crystallite interiors, which was attributed to the alleviation of diffusion restrictions and the suppression of coke formation at the Si-rich external surfaces.[22] Popov et al. reported that initial rates (per g) of butene oligomerization (1.5 MPa C_4H_8, 573 K) increased with increasing numbers of external Brønsted acid sites (per g) in MFI zeolites (Si/Al = 30), which was varied by decreasing the crystallite size (0.2–3 μm).[18] Corma et al. treated commercial MFI samples (Si/Al = 11–34) using post-synthetic treatments in acidic media (0.8 M oxalic acid, 2 h, 343 K) to preferentially dealuminate external surfaces and reported lower propene conversion (<65%) and faster catalyst deactivation for dealuminated MFI samples during propene oligomerization (4000 kPa C_3H_6, 473 K) at high conversions (X = 90%).[23]

Heterogeneous Al spatial distributions within a zeolite crystallite is referred to as "zoning", described as a gradient in H^+-site concentration from the center (or "core") to the external surface, and can originate during zeolite crystallization or be introduced via post-synthetic growth modifications.[24,25] The conditions of zeolite crystallization including temperature,[26] the silicon and aluminum sources[24] and SDAs used,[24,27] and post-synthetic treatments including acid or base leaching,[23,26,28] have been reported to influence the extent of Al zoning. Here, we adapted a two-step synthetic method from Rimer and co-workers[29] (details in Section S1, ESI†) to prepare core@shell MFI zeolite architectures and to investigate the effects of heterogeneous crystallite-scale H^+-site distributions on propene oligomerization rates and product selectivities. By creating a core@shell architecture, the boundary between regions in the zeolite crystallite containing high and low H^+-site density are more well-defined than the "zoned" regions that may form inherently during crystallization of a single crystallite, and thus can be resolved more accurately from TEM-EDX characterization. In such core@shell architectures (Si-MFI@Al-MFI), Al is preferentially located at external zeolite crystallite surfaces (in an "egg-shell"), while the center is catalytically inert and composed of silica (Fig. 1a). The shell thickness is expected to be the effective diffusion path length governing coupled reaction–diffusion networks, as this region is where the active H^+ sites are concentrated in the core@shell architecture.

To investigate the effect of crystallite-scale H^+-site distributions, we also synthesized two comparative MFI samples of similar bulk Si/Al ratio and more homogeneous Al spatial distributions, using synthesis gel compositions of tetrapropylammonium (TPA^+) and Na^+ reported to mitigate Al zoning (e.g., $TPA^+/(TPA^+ + Na^+) = 1$),[22] but crystallite sizes that are similar to either the overall crystallite radius or only the thickness of the shell in the Si-MFI@Al-MFI material (Fig. 1a–c). Samples are denoted MFI-X-Y, where X is the average crystallite size in nm and Y denotes the spatial distribution of acid sites (H = homogeneous, Z = zoned); salient characterization data are summarized in Table 1. MFI-183-Z (Si/Al = 56, 183 nm), MFI-158-H (Si/Al = 41, crystallite size = 158 nm), and MFI-22-H (Si/Al = 47, crystallite size = 22 nm) were synthesized using the procedures detailed in Section S1 (ESI†). Powder X-ray diffraction (XRD) and N_2 physisorption data show that all samples possess characteristics expected of the MFI framework (Fig. S1 and S2, ESI†).

The siliceous core (MFI-208) for Si-MFI@Al-MFI (MFI-183-Z) had a crystallite size of 208 ± 21 nm and showed a spherical morphology (Fig. S3a, ESI†). SEM images of MFI-183-Z showed a single crystal morphology of similar particle size (183 ± 25 nm, Table 1) as the siliceous core (208 ± 21 nm, Table 1), within error, and did not show a bimodal distribution of particle sizes (Fig. S3b and Section S4, ESI†), indicating the Al-rich shell grew on top of the siliceous core without parallel nucleation of a separate and distinct Al-MFI phase. XRD pat-
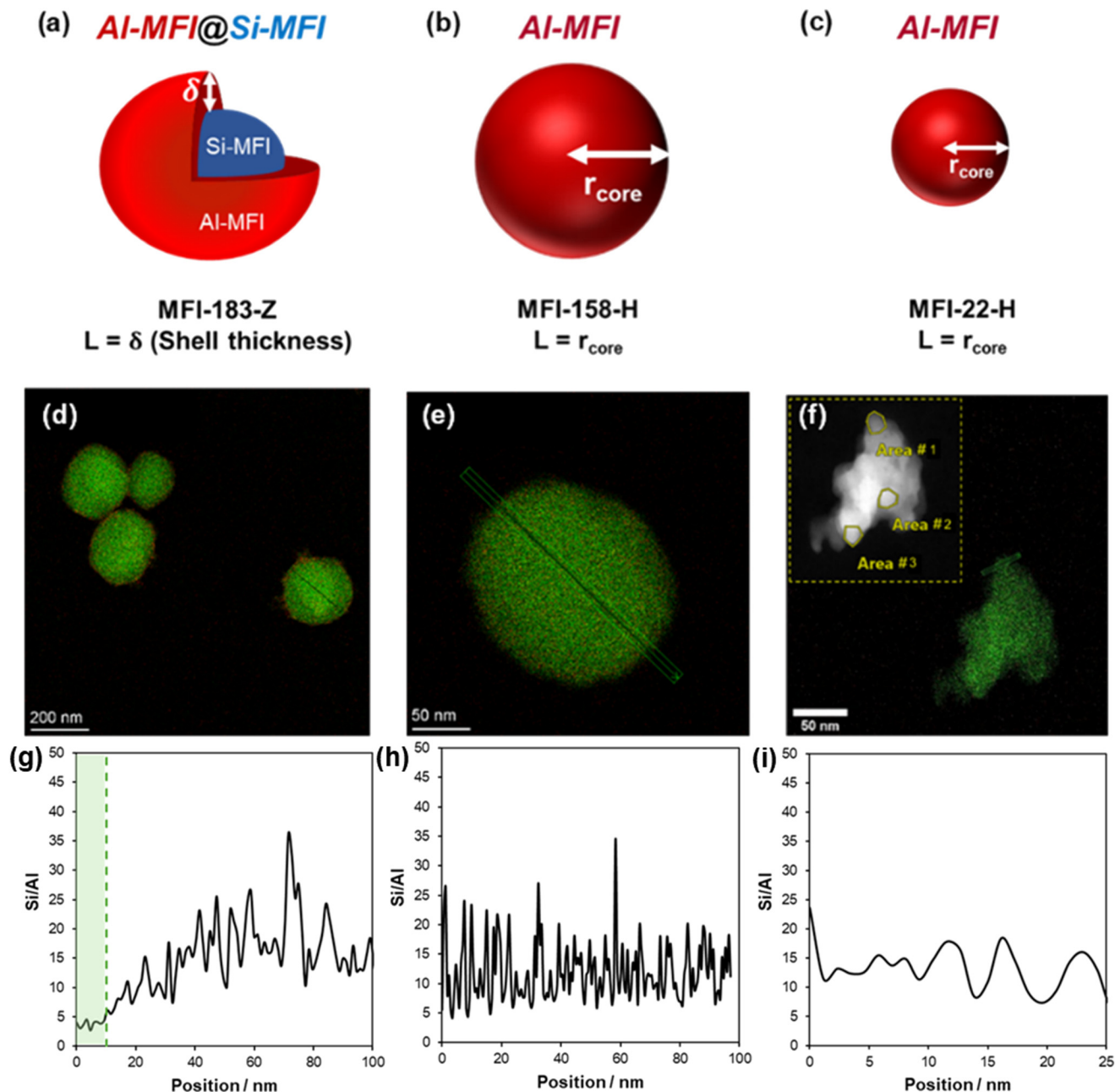
Fig. 1 Depiction of MFI samples with different diffusion path lengths (L) for (a) MFI-183-Z, (b) MFI-158-H, and (c) MFI-22-H. TEM-EDX images of Al (red) and Si (green) of (d) MFI-183-Z, (e) MFI-158-H, and (f) MFI-22-H (agglomerate of nanocrystallites). Inset in (f): HAADF mapping to highlight crystallites (yellow hexagonal shapes) in the agglomerated particles for MFI-22-H. TEM-EDX line-scans along the cross-section of a single particle of (g) MFI-183-Z (green line highlights the shell region), (h) MFI-158-H, and (i) area #1 in MFI-22-H.

terns (Fig. S1, ESI†) showed less intense (101) and (020) diffraction peaks after growth of the Al-rich shell onto the core (MFI-208) to form the Si-MFI@Al-MFI material (MFI-183-Z). These peaks index to the c-direction of MFI and have been attributed to coffin-like morphologies formed after shell growth;[30] thus, their lower relative intensities are consistent with the formation of spherical morphologies in Si-MFI@Al-MFI as observed by SEM (Fig. 1d). SEM images of MFI-158-H (Fig. S3c, ESI†) showed a spherical single-crystal morphology

with a monomial particle size distribution around 160 nm (Table 1). On the other hand, MFI-22-H shows nanosized crystallites (10–30 nm) agglomerated together, as observed by SEM (Fig. S3d, ESI†) and STEM-EDX (Fig. 1f), similar to the previous synthesis method using this germini-surfactant.[31] STEM-EDX mapping (Fig. 1d) and line scans (Fig. 1g) show an Al-shell thickness of ~10 nm in MFI-183-Z, evidenced by a Si/Al ratio that increases from ~5 at the surface to ~25 at the center, similar to previously reported syntheses;[21] in contrast,

Table 1 Physicochemical properties of MFI zeolite samples used in this study

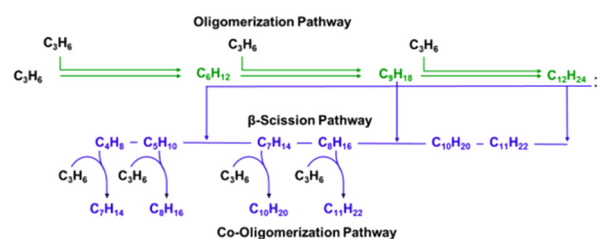| Sample[a]	Si/Al[b]	H_{tot}^+/Al[c]	H_{tot}^+/u.c.[c]	V_{micro}[d]/cm^3 g^{-1}	H_{ext}^+/H_{tot}[e]	Average crystallite diameter[f]/nm	Diffusion pathlength (L)/nm	Diffusion parameter (Ψ)/H_{tot}^+ nm^{-1}
MFI-208	∞	—	—	—	—	208 ± 21	—	—
MFI-183-Z	56	0.98	1.86	0.14	0.009	183 ± 25	10	2984
MFI-158-H	41	0.50	1.51	0.15	0.087	158 ± 23	79	1803
MFI-22-H	47	0.74	1.33	0.17	0.117[g]	22 ± 7	11	31

[a] Sample nomenclature: MFI-X-Y. X = average crystallite size in nm. Y denotes crystallite-scale Al distribution: Z = zoned, H = homogeneous. [b] Determined by ICP-OES. [c] Estimated by NH$_3$ TPD. [d] Micropore volumes (V_{micro}) determined by finding the minimum of the semilogarithmic plot of $\partial(V_{ads})/\partial(\ln(P/P_0))$ versus $\ln(P/P_0)$. [e] Estimated using the predicted H_{ext}^+ content from measured mesitylene benzylation rate constants (per total Al; Fig. S8†) and the total H^+ from NH$_3$ TPD (per g zeolite). Uncertainties range from ±25% to ±40%. [f] Estimated form SEM analysis of >30 particles. [g] Reported in Ezenwa et al.[32]

MFI-158-H (Fig. 1e and h) and MFI-22-H (Fig. 1f and i) have a more uniform Si/Al ratio as a function of single crystallite position. Additionally, XPS characterization of the MFI-183-Z sample showed an Si/Al ratio of 8 (Section S8, ESI†), similar to the value determined by STEM-EDX line scans (Fig. 1g), corroborating the presence of an Al-rich shell region. We note that the Si/Al ratio quantified by STEM-EDX is systematically lower than that measured by ICP-OES, likely because the former analyzes the composition of a single crystallite in the sample while the latter is representative of the bulk composition over all crystallites in the sample; however, the relative change in Si/Al ratio within the STEM-EDX line scans provide evidence of spatial heterogeneities of elemental composition within a given crystallite.

The number of H^+ sites (per g) was quantified by NH$_3$ temperature-programmed desorption (Fig. S4 and Section S5, ESI†) and all MFI samples had $H_{tot}^+/Al > 0.5$ as shown in Table 1. Mesitylene benzylation was used as a probe reaction to quantify the number of external acid sites, as described elsewhere by Ezenwa et al.[32] The fraction of external acid sites (H_{ext}^+/Al) was higher for MFI-22-H than the other samples (Table 1), as expected for its smaller crystallite size (<100 nm) that leads to higher surface area-to-volume ratios.[33]

The diffusion parameter was calculated using eqn (2) with L assumed to be equal to half of the crystallite diameter and is shown in Table 1. MFI-183-Z and MFI-158-H have similar Ψ values because these samples have similar H^+/u.c. and L. The Ψ value is lower for MFI-22-H because this sample has a smaller crystallite size. This set of samples allows investigating the influence of Al spatial distribution (i.e., zoning) and the diffusion path length on propene oligomerization catalysis. In the propene oligomerization reaction network, oligomerization forms alkene products with carbon numbers that are whole-number multiples of the monomer (termed "true oligomers") as shown in Scheme 1. These oligomer products can subsequently undergo β-scission reactions, producing alkenes with different carbon numbers. Additionally, propene can enter the reaction network through co-oligomerization reactions involving both propene and another alkene formed from a β-scission reaction, resulting in the generation of alkene products with carbon numbers that are non-integer multiples of 3.

Scheme 1 Propene oligomerization network on H-zeolites. Figure adapted with permission from Bickel and Gounder.[8] Oligomerization products are defined as those carbon numbers that are integer multiples of propene (i.e. $C_{3n}H_{6n}$, where n = 2, 3, 4, …).

Dimerization rates normalized by the number of H^+ sites quantified via ex situ NH$_3$ titration methods (H_0^+) were measured at 315 kPa C$_3$H$_6$ and 503 K as a function of time-on-stream for each of the MFI samples and were estimated from rates of product formation accounting for the formation of products other than dimers as shown in eqn (4):[8]

$$r_{dim} = r_6 + r_9 + r_{12} + \frac{1}{2}(r_4 + r_5 + r_7 + r_8 + r_{10} + r_{11}). \quad (4)$$

Dimerization rates (per H_0^+) were higher for MFI-22-H when compared to MFI-158-H (Fig. 2a) at these conditions (315 kPa C$_3$H$_6$, 503 K), as expected given the smaller crystallite size of MFI-22-H and its similar H^+-site density as MFI-158-H. Bickel et al. reported that propene dimerization rates (per H_0^+, 315 kPa C$_3$H$_6$, 503 K) systematically decreased with increasing crystallite size on MFI of fixed H^+-site density (H^+/u.c.), because the influence of intrazeolite diffusional restrictions imposed by the inorganic zeolite and its associated diffusion parameter (Ψ).[8,10] Dimerization rates (per H_0^+) for MFI-183-Z and MFI-158-H were similar, despite differences in their extent of Al zoning and the shorter effective diffusion path length in the "egg-shell" region (<10 nm) of MFI-183-Z than the average crystallite radius of MFI-158-H (79 nm; Fig. 2a); however, as observed from STEM-EDX line scans (Fig. 1d and e), the Al-rich shell region of MFI-183-Z has a 3× lower Si/Al ratio than its core or than MFI-158-H (~1.5 H^+/u.c., Table 1). Bickel et al. reported propene dimerization rates (per H_0^+) were lower on MFI samples of higher H^+-site density (e.g., 6 H^+/u.c.) than
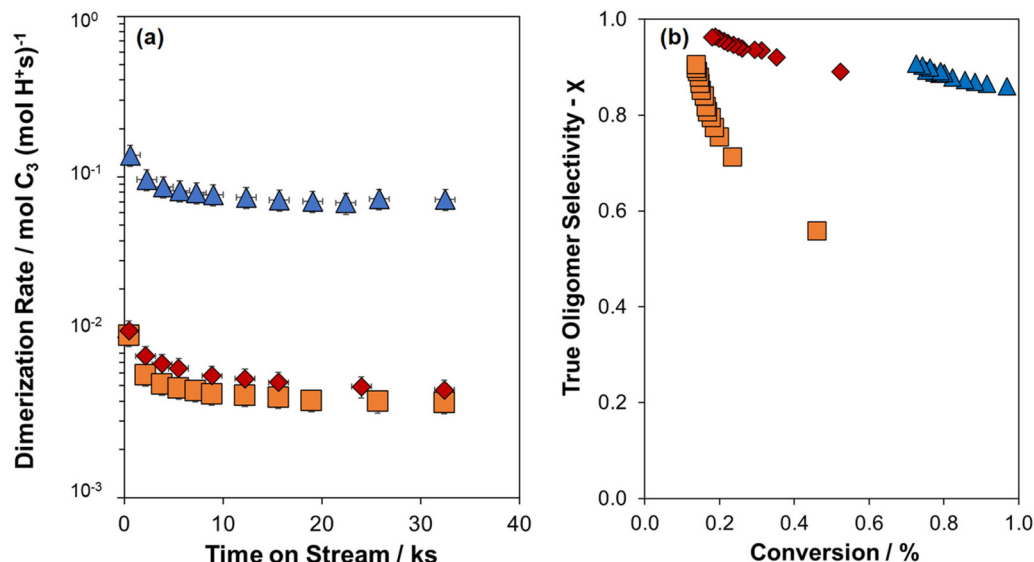
Fig. 2 (a) Propene dimerization rates (plotted on a logarithmic axis) measured at 503 K, 315 kPa C_3H_6 against time on stream for MFI-183-Z (♦), MFI-158-H (■), and MFI-22-H reproduced from Bickel *et al.*[10] (▲). (b) True oligomer selectivity (χ, eqn (3)) as a function of conversion at 503 K, 315 kPa C_3H_6 on MFI-183-Z (♦), MFI-158-H (■), and MFI-22-H (▲).

lower H^+-site density (*e.g.*, 1 H^+/u.c.) because H^+-site density influences the relative rates of oligomerization (chain-lengthening) and β-scission (chain-shortening) reactions, which lead to changes in the composition of the hydrocarbons that remain occluded within micropores during catalysis and, in turn, the diffusion restrictions this occluded organic phase introduces in addition to those imposed by the inorganic framework (described in Ψ).[10] Such changes to the composition of the intrapore occluded hydrocarbon phase should also be reflected in changes in the distribution of products that egress from zeolite crystallites, as quantified from reactor gas-phase effluents.

The propene oligomerization true oligomer selectivity (χ) is plotted in Fig. 2b as a function of conversion, which varied as MFI samples deactivated with time-on-stream. On all samples, χ increased as conversion decreased (Fig. 2b), consistent with higher fluid-phase concentrations of the primary product at higher conversions that increase rates of secondary reactions.[34] At a fixed conversion, χ values are lower for MFI-158-H than MFI-22-H, because smaller crystallites have a smaller diffusion parameter and thus a shorter intracrystalline residence time, facilitating the egression of oligomers from crystallites intact before undergoing β-scission events as reported by Sarazen *et al.*[7] Interestingly, at a fixed conversion, MFI-183-Z shows a significantly higher χ value than MFI-158-H despite their similar crystallite size, which we conclude reflects the "egg-shell" Al distribution (*i.e.*, Al zoning toward the surface) in MFI-183-Z that decreases the effective diffusion path length to a length scale characteristic of the shell thickness, and consequently decreases the effective diffusion parameter of the material. This results in similar χ values for MFI-183-Z and MFI-22-H (Fig. 2b), despite the latter having an 8× smaller crystallite size.

In summary, core@shell zeolite architectures provide a synthetic strategy to manipulate the spatial distribution of Al centers and their associated active H^+ sites independently of crystallite size, in turn affording influence over the rates and selectivities of coupled reaction–diffusion networks. Rates of propene oligomerization (per H_0^+) are characteristic of the local composition (H^+/u.c.) of the Al-rich shell region, and product selectivities are characteristic of the shorter diffusion path length characteristic of the shell thickness. As a result, zeolite materials with framework Al (and H^+-sites) zoned preferentially toward external surfaces allow suppressing the extent to which diffusion-enhanced secondary reactions would otherwise occur, which are β-scission reactions (chain-shortening) in the context of alkene oligomerization networks. These findings are reminiscent of the enhancement of Fischer–Tropsch synthesis rates and C_{5+} product selectivities on supported Co catalysts prepared in "egg-shell" architectures to alleviate CO diffusional restrictions.[35] Overall, these findings provide guidance on how to alter the spatial distribution of active sites within catalyst particles to influence the rates and selectivities of coupled reaction–diffusion networks.

Data availability

The data are available from the corresponding author on reasonable request.

Conflicts of interest

There are no conflicts to declare.

Acknowledgements

References

1 R. Khare, D. Millar and A. Bhan, A Mechanistic Basis for the Effects of Crystallite Size on Light Olefin Selectivity in Methanol-to-Hydrocarbons Conversion on MFI, *J. Catal.*, 2015, **321**, 23–31, DOI: **10.1016/j.jcat.2014.10.016**.

2 T. F. Degnan, The Implications of the Fundamentals of Shape Selectivity for the Development of Catalysts for the Petroleum and Petrochemical Industries, *J. Catal.*, 2003, **216**, 32–46, DOI: **10.1016/S0021-9517(02)00105-7**.

3 C. P. Nicholas, Applications of Light Olefin Oligomerization to the Production of Fuels and Chemicals, *Appl. Catal., A*, 2017, **543**, 82–97, DOI: **10.1016/j.apcata.2017.06.011**.

4 A. Corma, C. Martínez and E. Doskocil, Designing MFI-Based Catalysts with Improved Catalyst Life for Oligomerization to High-Quality Liquid Fuels, *J. Catal.*, 2013, **300**, 183–196, DOI: **10.1016/j.jcat.2012.12.029**.

5 J. E. Stanat, G. M. K. Mathys, D. W. Turner, J. C. Cheng, S. W. Beadle, C. M. C. Guajardo, R. Eijkhoudt, A. D. Godwin, E. E. Green, C. M. Yarbrough, R. F. Caers, C. B. Duncan and R. Y. Saleh, Oligomerization of olefins, *US Pat.*, US7425662B2, 2008.

6 D. A. Blain, N. M. Page and L. B. Young, Olefin oligomerization with surface modified zeolite catalyst, *US Pat.*, US5026933A, 1989.

7 M. L. Sarazen, E. Doskocil and E. Iglesia, Effects of Void Environment and Acid Strength on Alkene Oligomerization Selectivity, *ACS Catal.*, 2016, **6**(10), 7059–7070, DOI: **10.1021/acscatal.6b02128**.

8 E. E. Bickel and R. Gounder, Hydrocarbon Products Occluded within Zeolite Micropores Impose Transport Barriers That Regulate Brønsted Acid-Catalyzed Propene Oligomerization, *JACS Au*, 2022, **2**(11), 2585–2595, DOI: **10.1021/jacsau.2c00462**.

9 M. L. Sarazen, E. Doskocil and E. Iglesia, Catalysis on Solid Acids: Mechanism and Catalyst Descriptors in Oligomerization Reactions of Light Alkenes, *J. Catal.*, 2016, **344**, 553–569, DOI: **10.1016/j.jcat.2016.10.010**.

10 E. E. Bickel, S. Lee and R. Gounder, Influence of Brønsted Acid-Site Density on Reaction-Diffusion Phenomena That Govern Propene Oligomerization Rate and Selectivity in MFI Zeolites, *ACS Catal.*, 2023, **13**(2), 1257–1269, DOI: **10.1021/ACSCATAL.2C05184**.

11 G. Noh, S. I. Zones and E. Iglesia, Consequences of Acid Strength and Diffusional Constraints for Alkane Isomerization and β-Scission Turnover Rates and Selectivities on Bifunctional Metal-Acid Catalysts, *J. Phys. Chem. C*, 2018, **122**(44), 25475–25497, DOI: **10.1021/acs.jpcc.8b08460**.

12 P. Lu, S. Ghosh, M. Dorneles de Mello, H. S. Kamaluddin, X. Li, G. Kumar, X. Duan, M. Abeykoon, J. A. Boscoboinik, L. Qi, H. Dai, T. Luo, S. Al-Thabaiti, K. Narasimharao, Z. Khan, J. D. Rimer, A. T. Bell, P. Dauenhauer, K. A. Mkhoyan and M. Tsapatsis, Few-Unit-Cell MFI Zeolite Synthesized Using a Simple Di-Quaternary Ammonium Structure-Directing Agent, *Angew. Chem., Int. Ed.*, 2021, **60**(35), 19214–19221, DOI: **10.1002/anie.202104574**.

13 K. Ding, A. Corma, J. A. Maciá-Agulló, J. G. Hu, S. Krämer, P. C. Stair and G. D. Stucky, Constructing Hierarchical Porous Zeolites via Kinetic Regulation, *J. Am. Chem. Soc.*, 2015, **137**(35), 11238–11241, DOI: **10.1021/jacs.5b06791**.

14 L. Meng, B. Mezari, M. G. Goesten and E. J. M. Hensen, One-Step Synthesis of Hierarchical ZSM-5 Using Cetyltrimethylammonium as Mesoporogen and Structure-Directing Agent, *Chem. Mater.*, 2017, **29**(9), 4091–4096, DOI: **10.1021/acs.chemmater.7b00913**.

15 S. Adhikari, J. Zhang, K. Unocic, E. C. Wegener, P. Kunal, D. J. Deka, T. Toops, S. Sinha Majumdar, T. R. Krause, D. Liu and Z. Li, Direct 2,3-Butanediol Conversion to Butene-Rich C_{3+} Olefins over Copper-Modified 2D Pillared MFI: Consequence of Reduced Diffusion Length, *ACS Sustainable Chem. Eng.*, 2022, **10**(4), 1664–1674, DOI: **10.1021/acssuschemeng.1c07670**.

16 K. Kim, R. Ryoo, H.-D. Jang and M. Choi, Spatial Distribution, Strength, and Dealumination Behavior of Acid Sites in Nanocrystalline MFI Zeolites and Their Catalytic Consequences, *J. Catal.*, 2012, **288**, 115–123, DOI: **10.1016/j.jcat.2012.01.009**.

17 X. Zhang, D. Liu, D. Xu, S. Asahina, K. A. Cychosz, K. V. Agrawal, Y. Al Wahedi, A. Bhan, S. Al Hashimi, O. Terasaki, M. Thommes and M. Tsapatsis, Synthesis of Self-Pillared Zeolite Nanosheets by Repetitive Branching, *Science*, 2012, **336**(6089), 1684–1687, DOI: **10.1126/science.1221111**.

18 A. G. Popov, V. S. Pavlov and I. I. Ivanova, Effect of Crystal Size on Butenes Oligomerization over MFI Catalysts, *J. Catal.*, 2016, **335**, 155–164, DOI: **10.1016/j.jcat.2015.12.008**.

19 C. Wang, L. Zhang, X. Huang, Y. Zhu, G. Li, Q. Gu, J. Chen, L. Ma, X. Li, Q. He, J. Xu, Q. Sun, C. Song, M. Peng, J. Sun and D. Ma, Maximizing Sinusoidal Channels of HZSM-5 for High Shape-Selectivity to p-Xylene, *Nat. Commun.*, 2019, **10**(1), 4348, DOI: **10.1038/s41467-019-12285-4**.

20 T. T. Le, A. Chawla and J. D. Rimer, Impact of Acid Site Speciation and Spatial Gradients on Zeolite Catalysis, *J. Catal.*, 2020, **391**, 56–68, DOI: **10.1016/j.jcat.2020.08.008**.

21 T. T. Le, K. Shilpa, C. Lee, S. Han, C. Weiland, S. R. Bare, P. J. Dauenhauer and J. D. Rimer, Core-Shell and Egg-Shell Zeolite Catalysts for Enhanced Hydrocarbon Processing, *J. Catal.*, 2022, **405**, 664–675, DOI: **10.1016/j.jcat.2021.11.004**.

22 T. T. Le, W. Qin, A. Agarwal, N. Nikolopoulos, D. Fu, M. D. Patton, C. Weiland, S. R. Bare, J. C. Palmer, B. M. Weckhuysen and J. D. Rimer, Elemental Zoning Enhances Mass Transport in Zeolite Catalysts for Methanol to Hydrocarbons, *Nat. Catal.*, 2023, **6**, 254–265, DOI: **10.1038/s41929-023-00927-2**.

23 A. Corma, C. Martínez and E. Doskocil, Designing MFI-Based Catalysts with Improved Catalyst Life for $C_3^=$ and $C_5^=$ Oligomerization to High-Quality Liquid Fuels, *J. Catal.*, 2013, **300**, 183–196, DOI: **10.1016/J.JCAT.2012.12.029**.

24 R. Althoff, B. Schulz-Dobrick, F. Schüth and K. Unger, Controlling the Spatial Distribution of Aluminum in ZSM-5 Crystals, *Microporous Mater.*, 1993, **1**(3), 207–218, DOI: **10.1016/0927-6513(93)80079-A**.

25 R. von Ballmoos and W. M. Meier, Zoned Aluminium Distribution in Synthetic Zeolite ZSM-5, *Nature*, 1981, **289**(5800), 782–783, DOI: **10.1038/289782a0**.

26 W. Qin, Y. Zhou and J. D. Rimer, Deleterious Effects of Non-Framework Al Species on the Catalytic Performance of ZSM-5 Crystals Synthesized at Low Temperature, *React. Chem. Eng.*, 2019, **4**(11), 1957–1968, DOI: **10.1039/C9RE00231F**.

27 A. Chawla, R. Li, R. Jain, R. J. Clark, J. G. Sutjianto, J. C. Palmer and J. D. Rimer, Cooperative Effects of Inorganic and Organic Structure-Directing Agents in ZSM-5 Crystallization, *Mol. Syst. Des. Eng.*, 2018, **3**(1), 159–170, DOI: **10.1039/C7ME00097A**.

28 N. Danilina, F. Krumeich, S. A. Castelanelli and J. A. van Bokhoven, Where Are the Active Sites in Zeolites? Origin of Aluminum Zoning in ZSM-5, *J. Phys. Chem. C*, 2010, **114**(14), 6640–6645, DOI: **10.1021/jp1006044**.

29 A. Ghorbanpour, A. Gumidyala, L. C. Grabow, S. P. Crossley and J. D. Rimer, Epitaxial Growth of ZSM-5@Silicalite-1: A Core–Shell Zeolite Designed with Passivated Surface Acidity, *ACS Nano*, 2015, **9**(4), 4006–4016, DOI: **10.1021/acsnano.5b01308**.

30 M. Miyamoto, T. Kamei, N. Nishiyama, Y. Egashira and K. Ueyama, Single Crystals of ZSM-5/Silicalite Composites, *Adv. Mater.*, 2005, **17**(16), 1985–1988, DOI: **10.1002/adma.200500522**.

31 S. Lee and M. Choi, Unveiling Coke Formation Mechanism in MFI Zeolites during Methanol-to-Hydrocarbons Conversion, *J. Catal.*, 2019, **375**, 183–192, DOI: **10.1016/J.JCAT.2019.05.030**.

32 S. Ezenwa, G. M. Hopping, E. D. Sauer, T. Scott, S. Mack and R. Gounder, Quantification of Extracrystalline Acid Sites in MFI Zeolites after Post-Synthetic Treatments Using Mesitylene Benzylation Kinetics, *React. Chem. Eng.*, 2024, **9**, 1096–1112, DOI: **10.1039/D3RE00589E**.

33 M. Yamamura, K. Chaki, T. Wakatsuki, H. Okado and K. Fujimoto, Synthesis of ZSM-5 Zeolite with Small Crystal Size and Its Catalytic Performance for Ethylene Oligomerization, *Zeolites*, 1994, **14**(8), 643–649, DOI: **10.1016/0144-2449(94)90121-X**.

34 N. A. Bhore, M. T. Klein and K. B. Bischoff, The Delplot Technique: A New Method for Reaction Pathway Analysis, *Ind. Eng. Chem. Res.*, 1990, **29**(2), 313–316.

35 E. Iglesia, S. L. Soled, J. E. Baumgartner and S. C. Reyes, Synthesis and Catalytic Properties of Eggshell Cobalt Catalysts for the Fischer-Tropsch Synthesis, *J. Catal.*, 1995, **153**, 108–122.